

SMALL SCALE TENSILE TESTING OF TITANIUM ALLOYS

THESIS

Presented in Partial Fulfillment of the Requirements for
the Degree Master of Science in the
Graduate School of The Ohio State University

By

Katelun May, B.S.

• • • • •

Graduate Program in Materials Science and Engineering
The Ohio State University

2010

Master's Examination Committee:

Dr. Michael Mills, Advisor

Dr. Jim Williams

©

Copyright by

Katelun May

2010

Abstract

Precise characterization of individual slip system behavior is vital to understanding the strengthening mechanisms of many commercially important titanium alloys. However, limited data has been published on the mechanical properties of the alpha phase slip systems under tensile loading conditions as standard-sized single crystal specimens are difficult and expensive to produce. The development of a small scale testing system at The Ohio State University allowed for a quantitative assessment of tensile activation strength, hardening rate, and rate sensitivity of select HCP slip systems in Ti-6.7Al and Ti-6Al-2Sn-4Zr-2Mo-0.2Si. The results from this study have been compared to both the resolved shear stress magnitudes and anisotropy trends of previously reported data.

For John and our future.

Acknowledgments

First and foremost, I would like to acknowledge Prof. Michael Mills and Prof. Jim Williams for their guidance and encouragement throughout the entirety of this project. It has been enlightening to work with both gentlemen, and I am sincerely grateful for the warmth and understanding they have shown me during my time at OSU.

I would like to extend my thanks to all members of the Mills group – past and present – for the constant support, engaging debates, and endless good humor. Specifically, I would like to thank Bill Morgan for his assistance with sample preparation; without him, the “future work” section would be significantly larger.

My deepest gratitude is owed to Matt Brandes whose infinite patience, experience, and knowledge provided all of the groundwork (and most everything else) for this thesis. I genuinely appreciate all of the discussions we had, for his time was certainly valuable.

And to my family: your support has been priceless. I could never thank you enough.

Table of Contents

Abstract	ii
Acknowledgments.....	iv
Vita.....	v
List of Tables	viii
List of Figures	ix
Chapter 1: Tensile Testing of Alpha Phase Titanium.....	1
1.1: Introduction	1
1.2: Experimental Procedure	4
1.3: Micro-Tensile Test Results	7
1.3.1: Prismatic Slip Observations	7
1.3.2: Basal Slip Observations.....	11
1.3.3: $\langle c+a \rangle$ Observations.....	15
Chapter 2: Tensile Testing of Dual Phase Titanium.....	23
2.1: Introduction	23
2.2: Experimental Procedure	26
2.3: Micro-Tensile Test Results	27

2.3.1: Prismatic Slip Observations	27
2.3.1: Basal Slip Observations.....	30
2.4: Discussion	36
References.....	38
Appendix A: Experimental Procedure	40
A.1: Small Scale Tensile Test System	40
A.1.1: Digital Image Correlation.....	42
A.2: Generic Sample Preparation.....	44
A.3: Characterization	47
Appendix B: Nomenclature	49

List of Tables

Table 1.1: Alloying content of Ti-6.7Al single crystal rod ⁵	5
Table 1.2: Mechanical properties of Ti-6.7Al samples oriented for prismatic slip	11
Table 1.3: Mechanical properties of Ti-6.7Al samples oriented for basal slip	12
Table 1.4: Mechanical properties of Ti-6.7Al samples oriented for tension along $\langle c \rangle$	17
Table 1.5: Summary of hardening and rate sensitivities for Ti-6.7Al alpha phase slip systems in tension and compression.....	21
Table 2.1: Alloying content of Ti-6242Si single colony rod ⁵	26
Table 2.2: Mechanical properties of Ti-6242Si samples oriented for prismatic slip.....	30
Table 2.3: Mechanical properties of Ti-6242Si samples oriented for basal slip	33
Table 2.4: Summary of hardening and rate sensitivities for Ti-6242Si alpha phase slip systems in tension and compression.....	37

List of Figures

Figure 1.1: Compression CRSS values for alpha phase slip systems near 298K	2
Figure 1.2: Alpha phase micro-tensile sample orientations.....	6
Figure 1.3: Backscatter SEM image of {1010}<1120> slip in sample tested at $1.7 \times 10^{-4} \text{ s}^{-1}$ to a total strain of 19.9%	9
Figure 1.4: True stress-strain curves for samples oriented for prismatic slip.....	9
Figure 1.5: STEM foil orientation with respect to sample geometry and prismatic slip bands.....	10
Figure 1.6: Bright field STEM image of prismatic slip bands. Foil taken from sample shown in Figure 1.3. Zone axis: <1120>; $\mathbf{g}_{\langle 1011 \rangle}$	10
Figure 1.7: True stress-strain curves for samples oriented for basal slip.....	12
Figure 1.8: (a) Backscatter SEM image of (0001)<1120> slip in sample tested at $1.7 \times 10^{-4} \text{ s}^{-1}$ to a total strain of 1.2%; (b) Backscatter SEM image showing significant evidence of secondary slip in sample tested at $1.7 \times 10^{-4} \text{ s}^{-1}$ to a total strain of 30.4%	13
Figure 1.9: STEM foil orientation with respect to sample geometry and basal slip bands.....	14
Figure 1.10: STEM image of foil from sample with a total strain over 25%. Zone axis: <1101>; $\mathbf{g}_{\langle 0111 \rangle}$	14
Figure 1.11: High magnification STEM image of foil in Figure 1.10. Illustrates crack propagation deviation from basal planes.....	15
Figure 1.12: (a) Backscattered SEM image of slip bounded by a {1012}<1101> twin in sample taken to failure (6.1% total strain) at $1.7 \times 10^{-4} \text{ s}^{-1}$; (b) Backscattered SEM image of the identical twin bounded by <c+a>-type slip	16

Figure 1.13: True stress-strain curves for samples oriented for tension along $\langle c \rangle$	17
Figure 1.14: STEM foil orientation with respect to sample geometry	18
Figure 1.15: STEM micrograph showing evidence of two active $\langle c+a \rangle$ -type slip systems; Zone axis: $\langle 1120 \rangle$, $\mathbf{g}_{(0002)}$	18
Figure 1.16: Strength differential for alpha phase slip systems near 298K	19
Figure 2.1: Burgers orientation relationship between alpha and beta phases.	24
Figure 2.2: CRSS comparison for Ti-6242Si alpha phase slip systems near 298K.....	25
Figure 2.3: Backscattered SEM images of (a) $\langle a_1 \rangle$ prism slip morphology of sample tested at $1.7 \times 10^{-4} \text{ s}^{-1}$ to a failure strain of 28.9% and (b) $\langle a_2 \rangle$ prism slip morphology of sample tested at $1.7 \times 10^{-4} \text{ s}^{-1}$ to a failure strain of 17.6%	28
Figure 2.4: True stress-strain curves for samples oriented for $\langle a_1 \rangle$ prismatic slip	29
Figure 2.5: True stress-strain curves for samples oriented for $\langle a_2 \rangle$ prismatic slip	30
Figure 2.6: True stress-strain curves for samples oriented for $\langle a_1 \rangle$ basal slip	31
Figure 2.7: True stress-strain curves for samples oriented for $\langle a_2 \rangle$ basal slip	32
Figure 2.8: True stress-strain curves for samples oriented for $\langle a_3 \rangle$ basal slip	32
Figure 2.9: Backscatter SEM images illustrating (a) single slip regime of $\langle a_1 \rangle$ basal slip in sample tested at $1.7 \times 10^{-4} \text{ s}^{-1}$ to a failure strain of 9.8% and (b) evidence of secondary slip near shear failure in the same sample	34
Figure 2.10: Backscatter SEM image of (0001) $\langle a_2 \rangle$ slip morphology in sample tested at $1.7 \times 10^{-4} \text{ s}^{-1}$ to a failure strain of 14.9%	35
Figure 2.11: Backscatter SEM image of (0001) $\langle a_3 \rangle$ slip morphology in sample tested at $1.7 \times 10^{-4} \text{ s}^{-1}$ to a failure strain of 10.0%.	35
Figure 2.12: Tension vs. compression asymmetry for alpha phase slip systems in dual phase single colonies	36
Figure A.1: Illustration of small scale tensile test system	40
Figure A.2: "Bowtie" specimen with speckle pattern preloaded in grips	41

Figure A.3: (a) Square cross-section of laser cut sample; (b) Tapered cross-section of punch EDM sample45

Figure A.4: Rough edge and recast layer on sample perimeter (approx. 6 μm)45

Figure A.5: Micro-tensile sample geometries. All dimensions are in millimeters.46

Chapter 1: Tensile Testing of Alpha Phase Titanium

1.1: Introduction

Precise characterization of the deformation behavior of the hexagonal alpha phase is vital in understanding the strengthening contribution of the large volume fraction of this phase in many commercially important titanium alloys. Although there are six independent slip systems within the hexagonal close packed (HCP) structure, two are predominantly observed in titanium: $(0001)\langle 11\bar{2}0 \rangle$ and $\{10\bar{1}0\}\langle 11\bar{2}0 \rangle$ ^{1, 2}. Both systems account for deformation in $\langle a \rangle$ only; in order to satisfy continuity constraints, a deformation mechanism accommodating shape change along the c-axis must also exist. Twinning is frequently observed in titanium alloys; however, alpha-stabilizing elements, such as aluminum and oxygen, have been shown to suppress twin formation permitting $\langle c+a \rangle$ -type slip to occur². Therefore it is of great interest to not only characterize $\langle a \rangle$ -type basal and prism systems but also to evaluate the primary $\langle c+a \rangle$ slip system.

Efforts have been made to quantify the mechanical behavior of the important HCP slip systems through compression tests using single crystals oriented to achieve maximum shear stress along the desired slip system. Presented in Figure 1.1 is a comparison of published critical resolved shear stresses (CRSS) required to activate basal, prismatic, and $\langle c+a \rangle$ -type slip in various Ti-Al alloys. The plot shows the CRSS

near 298K of alloys with aluminum concentrations mimicking those found in common structural alloys (3-7 wt% Al)^{2, 3, 4, 5}.

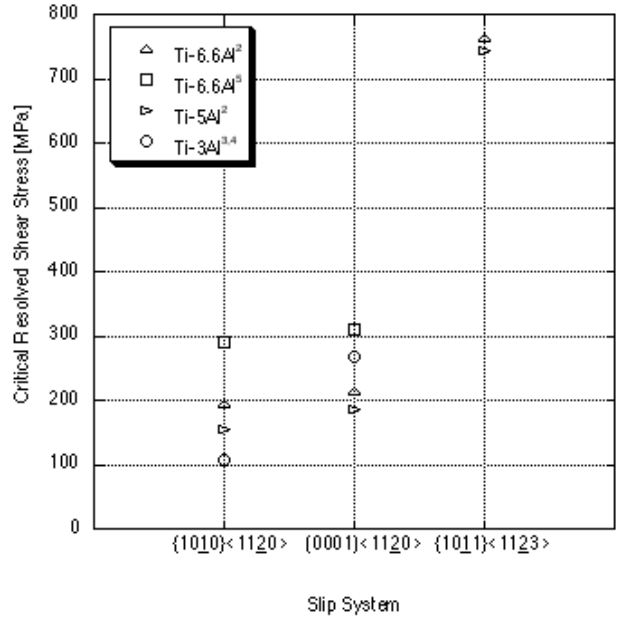


Figure 1.1: Compression CRSS values for alpha phase slip systems near 298K

Moderate yield strength anisotropy was observed between basal and prismatic slip activation. Additionally, physical inspection of the compression samples revealed distinct plastic deformation behavior for each slip system. Low strain prismatic slip near 298K was repeatedly characterized by fine planar slip bands consisting of high density, relatively straight screw dislocations^{2, 3}. In contrast, basal dislocations occurred in coarse, well-defined slip bands with evidence of cross-slip by screw dislocations onto prism planes^{2, 4}. The notable lack of observed edge components implies that the low-mobility screw dislocations control the mechanical response of the slip system. Thus, for <a>-type slip the anisotropy is attributed to the complex core of <1120> screw dislocations⁶. Bond-

order potential calculations by Girshick *et al.* on pure titanium show that the screw core is non-planar, and may spread on either the basal or prism planes depending on the local energy conditions⁷. The magnitude of the $\langle a \rangle$ -type slip system stress asymmetry decreases with increased aluminum content demonstrating that the core behavior is sensitive to alloying elements^{2, 3, 4}. A significant increase in the complexity of the core is also observed in the increased affinity for basal slip in systems with greater aluminum and oxygen concentrations⁶.

Significant CRSS anisotropy was also detected between the $\langle a \rangle$ -type and $\langle c+a \rangle$ -type slip systems. Compression along the c-axis, which resulted in a zero resolved shear stress on $\langle a \rangle$ -type systems, induced $\langle c+a \rangle$ -type slip primarily on the $\{10\bar{1}1\}$ and $\{11\bar{2}2\}$ planes². The resulting dislocations were mainly edge in character since these components have limited mobility due to the out-of-plane displacements required for progression along $\langle 11\bar{2}3 \rangle$ ⁶. Atomistic simulations on the behavior of the $\{11\bar{2}2\}\langle 11\bar{2}3 \rangle$ core confirmed the complex, non-planar nature of the $\langle c+a \rangle$ dislocation⁸.

In addition to the marked difference in activation strength between the tested alpha phase slip systems, other plastic response parameters – such as hardening rate and rate sensitivity – may also be slip-system dependent. Under compressive loading, prismatic slip exhibited no hardening or softening while basal slip showed moderate hardening, and samples oriented for $\langle c+a \rangle$ -type slip displayed strong hardening tendencies⁵. The same compression strain rate sensitivities are reported for basal and prismatic slip ($m_B = m_P = 0.02$)⁶. A rate sensitivity study has not been completed for $\langle c+a \rangle$ oriented samples.

Considerable variation has been observed in the plastic flow of select HCP slip systems in compression. However, limited data is available on the mechanical properties of the same systems under tensile loading conditions. Standard-sized tensile specimens are rarely used due to the difficulty and expense of producing sufficiently large single crystals. Nonetheless, tension-compression strength differentials have been reported for highly-textured two-phase titanium systems⁹. Neeraj *et al.* proposed that the complex $\langle a \rangle$ -type screw core assumes different configurations based on the applied stress state¹⁰. In order to quantitatively assess the stress asymmetry and further characterize the alpha phase slip systems small scale testing must be employed. Savage and Brandes performed preliminary micro-tensile studies on single crystal Ti-6.6Al samples using a micro-tensile rig first developed by Sharpe *et al.* at John Hopkins University^{5, 6, 11}. Both studies attempted to identify the tensile CRSS for the basal, prismatic, and $\langle c+a \rangle$ -type slip systems. However, the stress-stain curves exhibited atypical features including a non-linear modulus and the lack of a well-defined yield point, resulting in questionable accuracy. As such, the tensile activation strengths and rate sensitivities of the selected HCP slip systems will be quantified using an updated small scale testing system developed at The Ohio State University (see Appendix A).

1.2: Experimental Procedure

In order to thoroughly characterize the tensile response of the alpha phase slip systems, single crystal micro-tensile samples were created from a rod of single phase Ti-6.7Al. Initially fabricated by Duriron, Inc., large crystals were grown using a vertical

float-zone technique at Wright Patterson Air Force Base courtesy of Dr. Michael Uchic. This alloy was chosen due to the relative ease with which large alpha phase crystals could be formed. The composition, which closely represents the alloying content of the alpha phase in many commercial titanium alloys, can be found in Table 1.1. The oxygen and hydrogen values listed in this table were obtained using an inert gas fusion technique, while the aluminum content was measured using plasma emission spectrometry. The weight percent of all other elements are reported directly from previous accounts of the material composition⁵.

Element	Composition [wt%]
Al	6.72
O	0.19
Fe	0.067
Cu	0.054
Ni	< 0.05
C	0.0157
N	0.006
H	0.0088

Table 1.1: Alloying content of Ti-6.7Al single crystal rod⁵

Three unique slip systems were selected for tensile testing: $(0001)\langle 11\bar{2}0 \rangle$, $\{10\bar{1}0\}\langle 11\bar{2}0 \rangle$, $\langle c+a \rangle$ -type. The basal and prismatic slip samples were oriented to maximize the Schmid factor of the desired slip plane. The polished face of the samples contained both the normal to the slip plane and the shear vector. Due to the relatively high critical stress required to activate $\langle c+a \rangle$ -type slip, this set of samples was oriented for zero resolved shear stress along the a-direction. The orientation of each set of samples is illustrated in Figure 1.2.

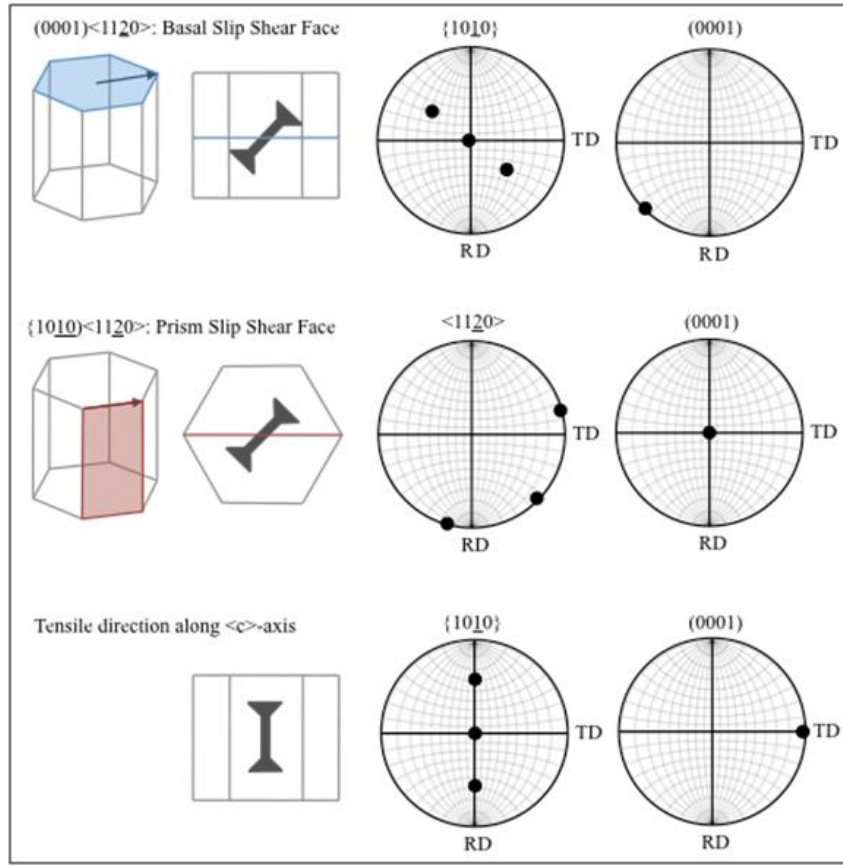


Figure 1.2: Alpha phase micro-tensile sample orientations

As this tensile study compliments the single crystal compression tests performed by Savage, the Ti-6.7Al samples were heat treated to replicate the same short range order conditions⁵. Prior to laser cutting the samples, slices of Ti-6.7Al were heat treated at 1173K for 24 hours and then air-cooled. Further details on sample preparation and the experimental procedure are outlined in Appendix A.

The critical resolved shear stress was obtained by multiplying the 0.2% offset yield stress by the Schmid factor for a given sample. The hardening rate of the single-slip region (n) for each monotonic strain rate tensile test was calculated using:

$$n = \frac{\log_{10}(\sigma_1/\sigma_2)}{\log_{10}(\dot{\epsilon}_1/\dot{\epsilon}_2)} \Big|_{\dot{\epsilon}}$$

Specifically, linear interpolation was performed on the plastic strain, single-slip region of a monotonic strain rate curve plotted on logarithmic axes. Strain rate sensitivity (m) was calculated in the single-slip regime using the true stress associated with one-percent plastic strain. To obtain m , a trend line was fit to a logarithmic plot of the stresses versus the corresponding strain rates:

$$m = \frac{\log_{10}(\sigma_1/\sigma_2)}{\log_{10}(\dot{\epsilon}_1/\dot{\epsilon}_2)} \Big|_{\epsilon_{pl}}$$

1.3: Micro-Tensile Test Results

1.3.1: Prismatic Slip Observations

Fine, uniform slip bands – such as those shown in Figure 1.3 – characterized high strain prismatic slip under tensile loading conditions. Slip traces were distributed homogeneously across the entire gage section; additionally, the minimal localization was further reflected in the relatively low flow softening observed in the stress-strain curves presented in Figure 1.4. It should be noted that the monotonic strain rate tests shown here were based on VIC2D strain measurements, and as such do not contain the near-failure portion of the curve (see Section A.1.1). Quantitative results for each test are summarized in Table 1.2. The strain rate sensitivity at one percent plastic strain is $m = 0.086$.

Further examination of the high-strain plastic region was completed using scanning transmission electron microscopy (STEM) on a foil extracted from the micro-tensile specimen using a focused ion beam, as discussed in Section A.3. The orientation of this foil with respect to the sample geometry and the activated slip bands is shown in Figure 1.5. The STEM image revealed dense, tortuous slip bands with significant evidence of basal cross-slip, as shown in Figure 1.6. This tensile slip character agrees well with observations by Williams *et al.* on prismatic slip in compression, which showed that the active slip bands in alloys with relatively high aluminum content were thinner and had higher dislocation densities than alloys with lower weight percent aluminum². Screw dislocation arrays can also be seen exterior to the debris-laden bands in Figure 1.6. The presence of these arrays implies that the relatively low softening may be a direct result of the lower stresses required to move a dislocation through the virgin matrix rather than through the crowded slip bands.

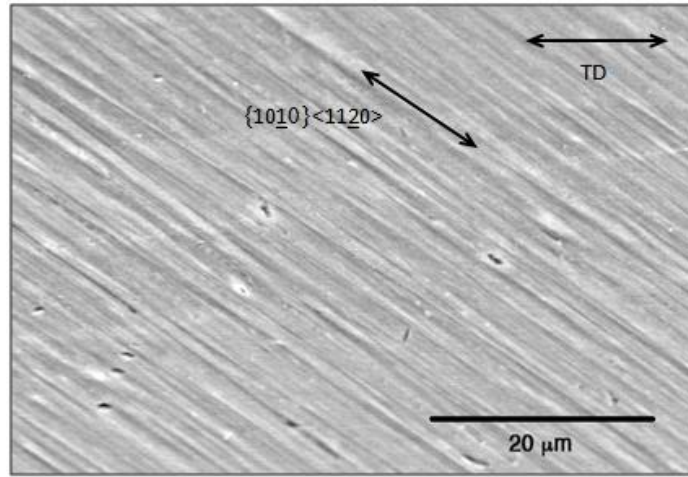


Figure 1.3: Backscatter SEM image of $\{10\bar{1}0\} \langle 11\bar{2}0 \rangle$ slip in sample tested at $1.7 \times 10^{-4} \text{ s}^{-1}$ to a total strain of 19.9%

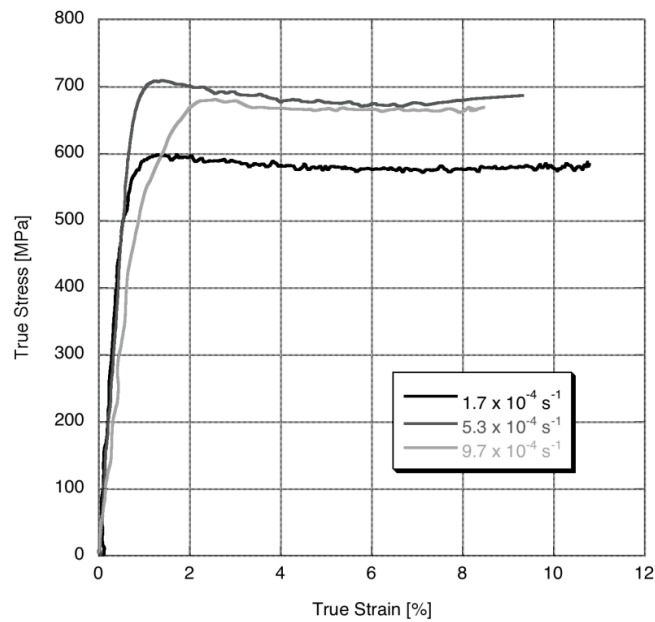


Figure 1.4: True stress-strain curves for samples oriented for prismatic slip

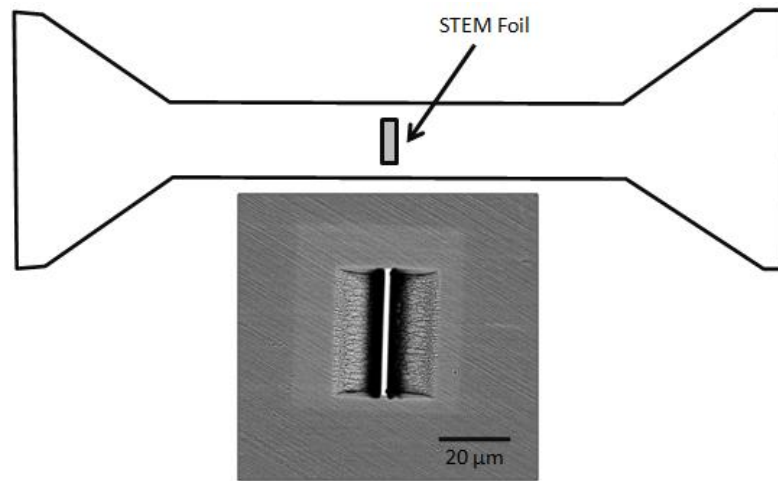


Figure 1.5: STEM foil orientation with respect to sample geometry and prismatic slip bands

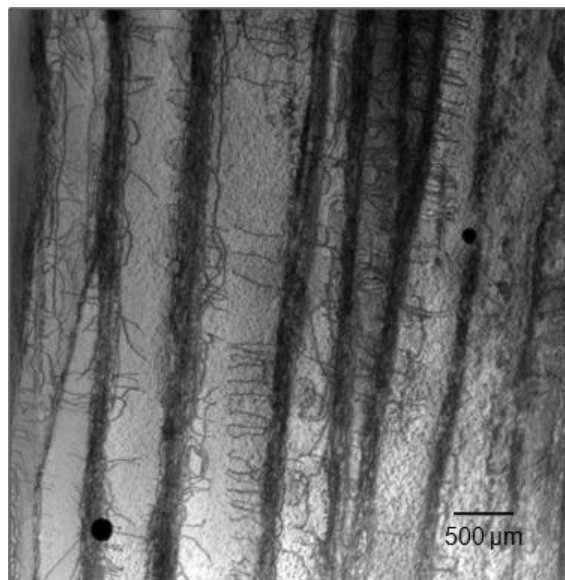


Figure 1.6: Bright field STEM image of prismatic slip bands. Foil taken from sample shown in Figure 1.3. Zone axis: $\langle 11\bar{2}0 \rangle$; $\mathbf{g}_{\langle 10\bar{1}1 \rangle}$

Strain Rate [s ⁻¹]	0.2% Offset Yield [MPa]	Upper Yield Point [MPa]	CRSS [MPa]	Total Strain [%]	n [$\times 10^{-2}$]
1.7×10^{-4}	561	588	279	34.0 **	-2.4
5.3×10^{-4}	687	698	342	35.2 **	-3.5
9.7×10^{-4}	556	662	277	29.8 **	-0.8

Table 1.2: Mechanical properties of Ti-6.7Al samples oriented for prismatic slip

** Sample was stopped before failure to allow for a final strain measurement using the optical system.

1.3.2: Basal Slip Observations

The micro-tensile response for three samples oriented for basal slip is shown in Figure 1.7, and the resultant mechanical properties are tabulated in Table 1.3. The curves presented in Figure 1.7 were calculated from VIC2D strain measurements, and therefore do not contain the near-failure portion of the curve (see Section A.1.1). Calculations indicated the strain rate sensitivity at one percent plastic strain was $m = 0.155$, nearly one order of magnitude higher than the reported values of compression rate sensitivity for the same slip system⁶.

Severe softening followed by moderate hardening characterized the plastic region of each monotonic strain rate test. The small strain region consisted of a single slip regime of well-defined <a>-type basal slip bands. At higher strains, samples hardened as secondary slip developed between the primary basal slip bands. This difference in the slip morphology between low strain and high strain regions can be seen in Figure 1.8. To further examine the slip character using STEM, a foil was extracted across both the primary and secondary slip region, as shown in Figure 1.9. The details of this process are presented in Section A.3. The low-magnification STEM micrograph, shown in Figure 1.10, revealed that the basal slip bands are broader and have lower dislocation density

than their prism counterparts. The regions of secondary slip, which appear to be a first or second-order pyramidal system, can be seen overlapping the primary basal bands. Additional work must be completed to identify the systems. Evidence of tearing was observed near the edge of the secondary slip, as seen in Figure 1.11. It is significant to note that the cracking propagates approximately 5-6 degrees off the basal plane.

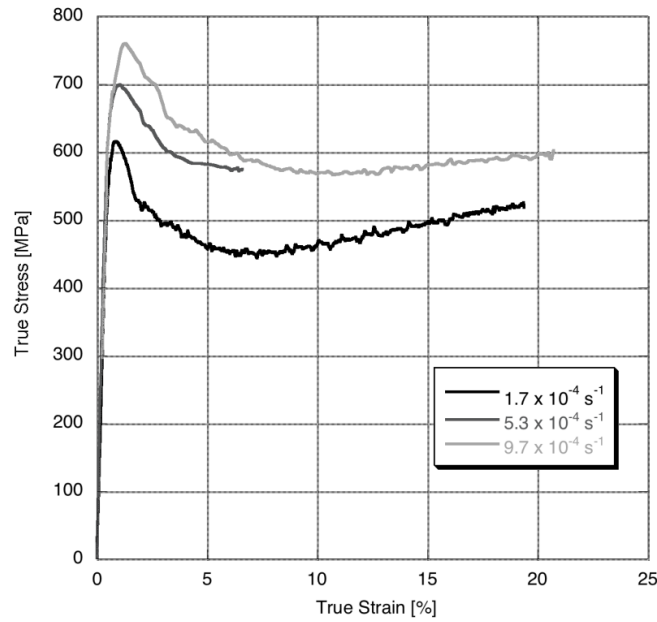


Figure 1.7: True stress-strain curves for samples oriented for basal slip

Strain Rate [s ⁻¹]	0.2% Offset Yield [MPa]	Upper Yield Point [MPa]	CRSS [MPa]	Total Strain [%]	n [×10 ⁻²]
1.7 × 10 ⁻⁴	595	609	293	30.4 **	-14.8
1.7 × 10 ⁻⁴	538	592	265	1.8 *	-14.6
5.3 × 10 ⁻⁴	662	692	326	38.3 **	-14.0
9.7 × 10 ⁻⁴	684	750	337	39.0 **	-13.1

Table 1.3: Mechanical properties of Ti-6.7Al samples oriented for basal slip.

* Sample was stopped prematurely to examine the small strain region.

** Sample was stopped before failure to allow for a final strain measurement using the optical system.

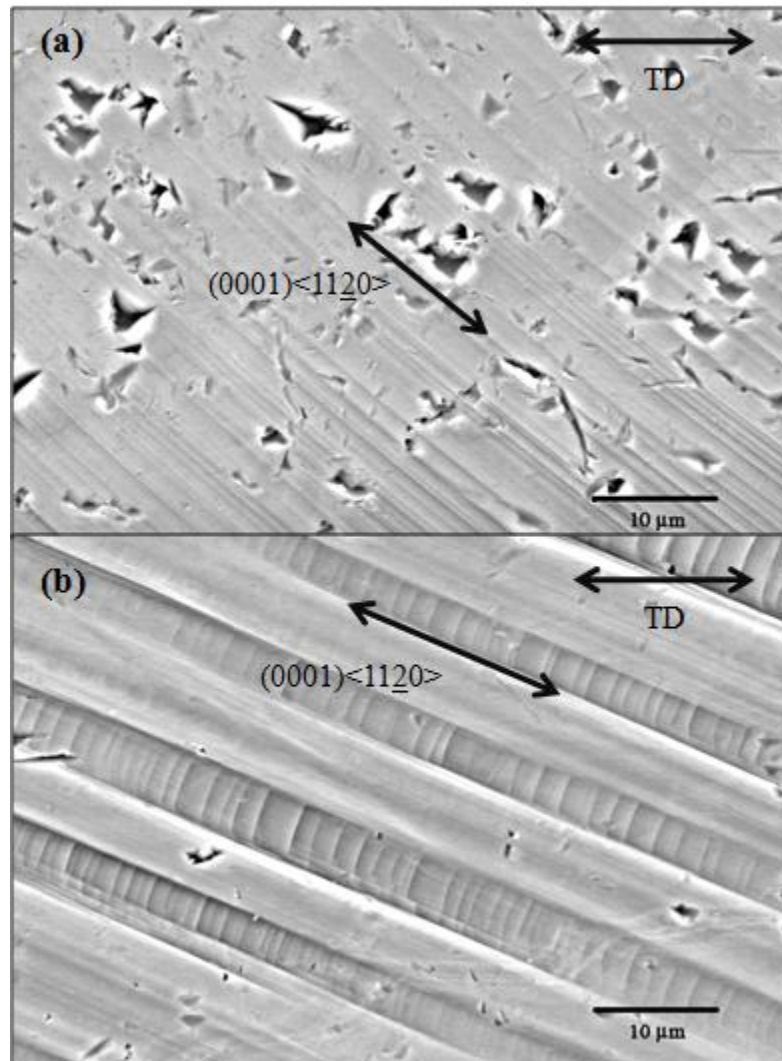


Figure 1.8: (a) Backscatter SEM image of $(0001)\langle 11\bar{2}0 \rangle$ slip in sample tested at $1.7 \times 10^{-4} \text{ s}^{-1}$ to a total strain of 1.2%; (b) Backscatter SEM image showing significant evidence of secondary slip in sample tested at $1.7 \times 10^{-4} \text{ s}^{-1}$ to a total strain of 30.4%

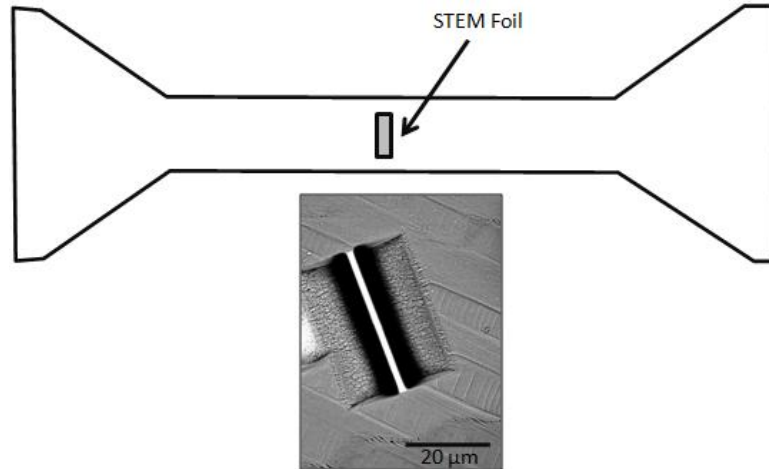


Figure 1.9: STEM foil orientation with respect to sample geometry and basal slip bands



Figure 1.10: STEM image of foil from sample with a total strain over 25%. Zone axis: $\langle 1\bar{1}01 \rangle$; $\mathbf{g}_{\langle 011 \rangle}$

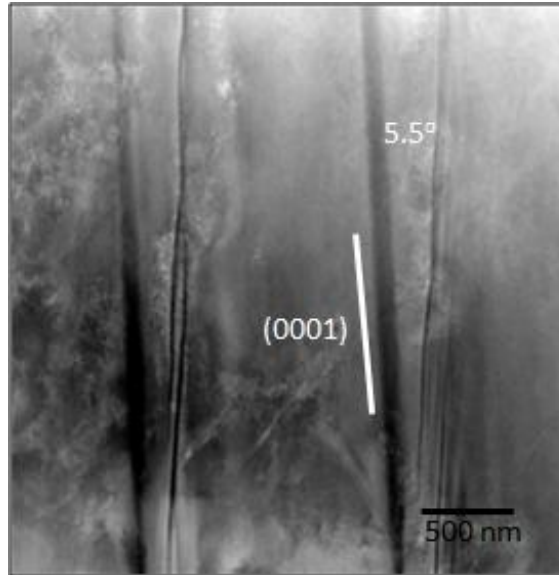


Figure 1.11: High magnification STEM image of foil in Figure 1.10. Illustrates crack propagation deviation from basal planes.

1.3.3: $\langle c+a \rangle$ Observations

In the Ti-6.7Al single crystal samples oriented for tension along $\langle c \rangle$, significant twinning was discernible on all specimens. Twin formation began at stress levels very close to those required for $\langle c+a \rangle$ -type slip activation. In Figure 1.12(a) the $\{10\bar{1}2\}\langle 11\bar{0}1 \rangle$ twin appears to precede slip; however, Figure 1.12(b) portrays the same twin bounded by slip bands. Moderate hardening is observed in the stress-strain curves, presented in Figure 1.13, as both twins and slip continue to be activated throughout the plastic regime. Figure 1.15, a STEM micrograph of the un-twinned matrix (foil orientation shown in Figure 1.14), reveals activation of two distinct $\langle c+a \rangle$ -type slip systems. Additional work must be completed to identify the systems.

Table 1.4 presents the quantitative results of these micro-tensile tests. CRSS values, resolved along $\{10\bar{1}1\}\langle 11\bar{2}3 \rangle$, are presented under the assumption that $\langle c+a \rangle$ -

type slip occurs first. The average strain rate sensitivity of this orientation is minimal: $m = 0.015$.

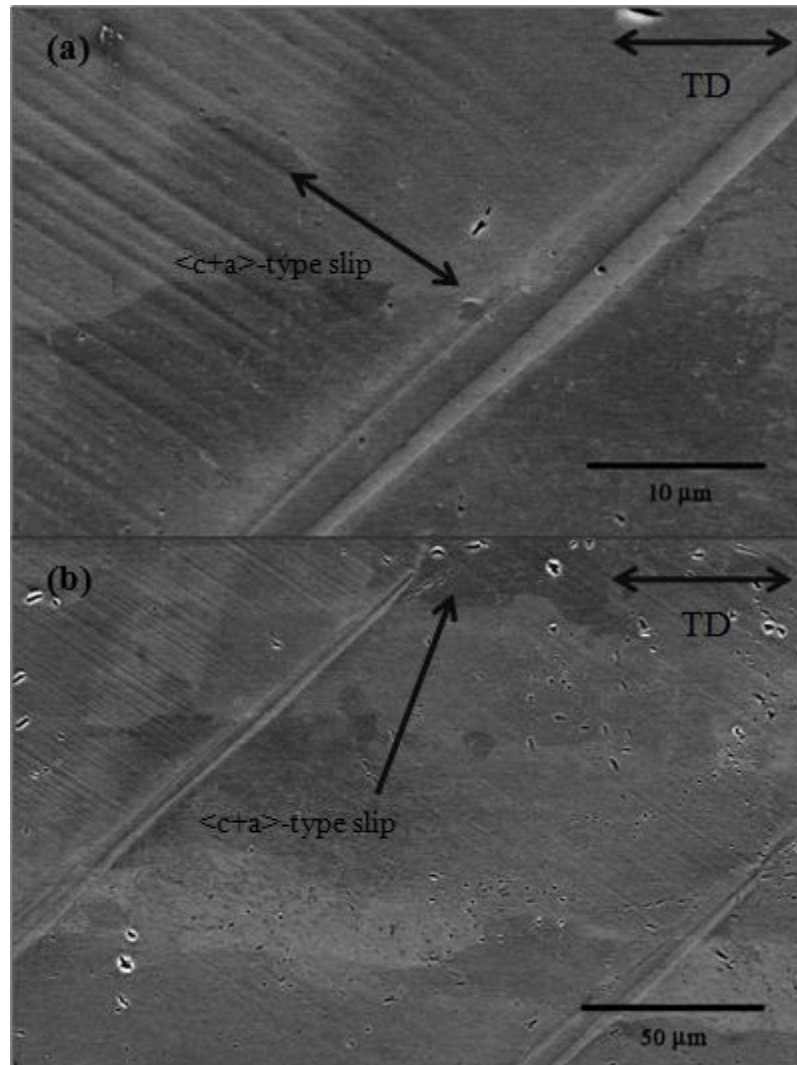


Figure 1.12: (a) Backscattered SEM image of slip bounded by a $\{10\bar{1}2\}\langle 1\bar{1}01 \rangle$ twin in sample taken to failure (6.1% total strain) at $1.7 \times 10^{-4} \text{ s}^{-1}$; (b) Backscattered SEM image of the identical twin bounded by $\langle c+a \rangle$ -type slip

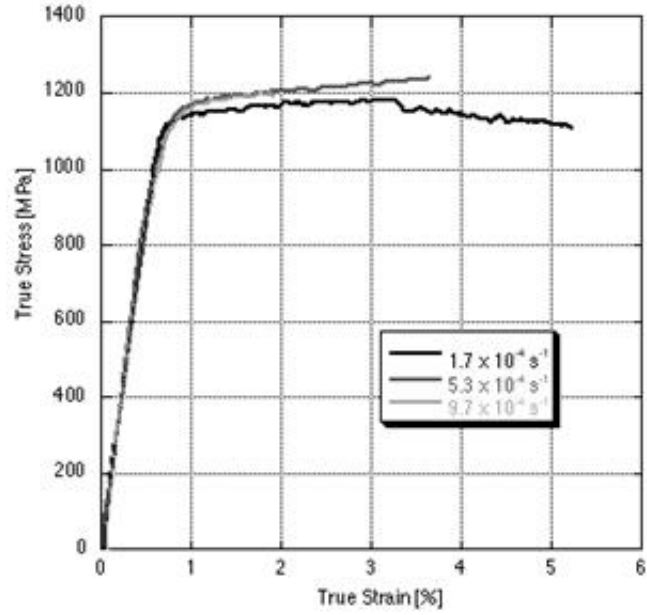


Figure 1.13: True stress-strain curves for samples oriented for tension along $\langle c \rangle$

Strain Rate [s^{-1}]	0.2% Offset Yield [MPa]	Upper Yield Point [MPa]	CRSS [MPa]	Total Strain [%]	n [$\times 10^{-2}$]
1.7×10^{-4}	1121	1150	460	6.1	3.3
1.7×10^{-4}	1152	1173	472	2.2 *	3.6
5.3×10^{-4}	1145	1191	470	8.9	3.9
9.7×10^{-4}	1128	1174	462	4.2	4.2

Table 1.4: Mechanical properties of Ti-6.7Al samples oriented for tension along $\langle c \rangle$

* Sample was stopped prematurely to examine the small strain region.

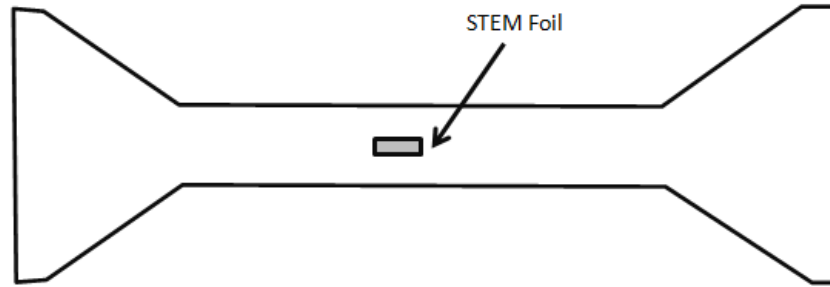


Figure 1.14: STEM foil orientation with respect to sample geometry

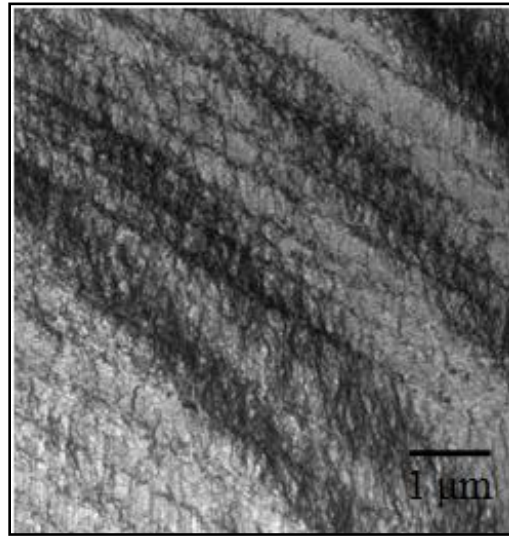


Figure 1.15: STEM micrograph showing evidence of two active $\langle c+a \rangle$ -type slip systems;
Zone axis: $\langle 11\bar{2}0 \rangle$, $\mathbf{g}_{(0002)}$

1.4: Discussion

The critical resolved shear strengths for samples taken to (near) failure at $1.7 \times 10^{-4} \text{ s}^{-1}$ are presented with the previously published compression results in Figure 1.16. The limited anisotropy between the $\langle a \rangle$ -type slip systems agreed well with data presented by Williams *et al.* showing the resolved shear strength for prismatic and basal slip converging with increasing aluminum content². From the literature prismatic slip was expected to activate at the lowest stress levels, yet in this study basal slip has the smallest

CRSS, likely due to a lower proportional limit exhibited by the basal system. This initial region of plastic deformation was thought to be due to cracking of the recast layer on the perimeter prior to slip initiation in the bulk of the sample. As the CRSS values were based on the 0.2% offset yield, the basal strength appeared artificially low. Comparison of the upper yield points revealed a higher strength for the basal system as compared to the prismatic system. Additionally, compared to the homogenous slip morphology seen in the prism samples, basal slip has fewer and coarser slip bands and may have been more influenced by the rough recast sidewalls (shown in Figure A.4). It should be noted that the recast layer may have inhibited $\langle a \rangle$ -type edge dislocations from exiting the specimens.

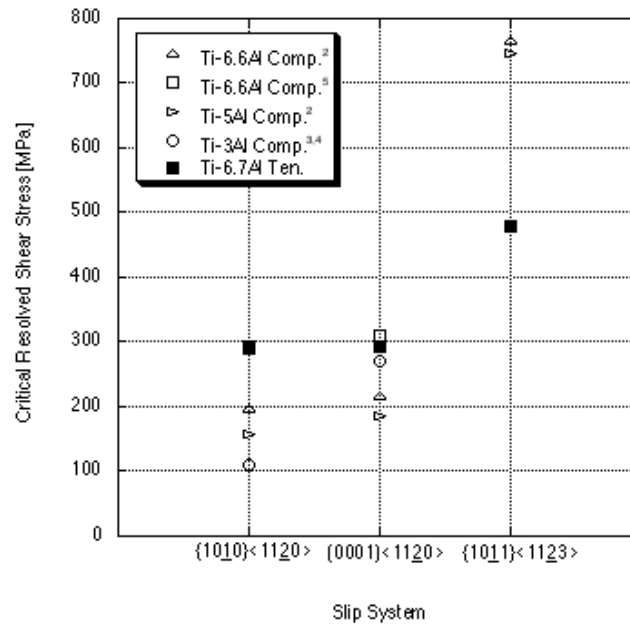


Figure 1.16: Strength differential for alpha phase slip systems near 298K

When comparisons were drawn between this study and the compression counterparts, the magnitude of the strength differential appeared relatively modest. An increase in the flow strength of a material is often reported for small scale tests due to extrinsic size effects on plasticity^{12, 13}. However, Dimiduk *et al.* have shown that the CRSS and hardening characteristics of single-crystal pure nickel compression samples with a diameter greater than 40 microns are on the order of those experienced by bulk specimens (< 30% difference)¹². The authors also stated that samples with diameters greater than 300 microns are “nearly bulk-like” with sufficient volume to avoid dislocation exhaustion and significant effects due to free surface interaction. Furthermore, the modulus measurements on the small scale samples oriented with the tensile direction along the <c>-axis ($E_{\text{avg}} = 165 \pm 7$ GPa) fell within the range presented by Fisher and Ranken for pure titanium obtained using acoustic wave propagation ($E = 180 \pm 18$ GPa)¹⁴. The strength values may have been influenced by the sample preparation techniques outlined in Appendix A. Specifically, removing the rough recast layer from the sidewalls of the gage length and obtaining a pristine surface finish may have altered the values presented above.

Table 1.5 compares the hardening values and rate sensitivities resulting from this micro-tensile study to values from previous compression tests. The compression n values were calculated directly from compression curves produced by Savage using the same method as was used to calculate the hardening rate of the tension tests (discussed in Section 1.2)⁵.

Slip System	n_{TEN}	n_{COMP}	m_{TEN}	m_{COMP}
{1010}<1120>	-0.024	0.010	0.086	0.020 ⁶
(0001)<1120>	-0.148	0.132	0.155	0.020 ⁶
Loaded along <c>	0.033	0.139	0.015	-

Table 1.5: Summary of hardening and rate sensitivities for Ti-6.7Al alpha phase slip systems in tension and compression. Hardening rates are provided for tests at strain rate near $1.7 \times 10^{-4} \text{ s}^{-1}$; tension rate sensitivity values were calculated at one percent plastic strain.

Softening was observed in the tensile true stress-strain response of the samples oriented for prismatic slip; the softening rate is on the same order of magnitude as the hardening rate of the compression data. Samples oriented for basal slip exhibited a significantly different response under tensile conditions as compared to compression. Not only did basal slip exhibit a much higher rate dependency in tension, it also displayed considerable softening in the single-slip regime. A single crystal loaded along the <c>-axis displayed hardening under both tension and compression conditions, although the hardening rate was noticeably higher in compression. Additional work is required to assess the underlying causes of the tension-compression asymmetry of the three alpha phase slip systems.

In addition to identifying the activated slip systems in each series of samples and further exploring the load direction asymmetry, the effects of short-range order could easily be investigated through rapid quenching of the micro-tensile sample after a solution heat treatment. Additional studies should also focus on characterization of the damage layer due to the laser cutting process. Other micro-tensile sample cutting options,

such as wire EDM, should be explored to reduce the rough recast layer on the sidewalls of the sample while maintaining a square cross-section.

Chapter 2: Tensile Testing of Dual Phase Titanium

2.1: Introduction

Structural titanium alloys are divided into classes based on the type and quantity of phases present in the microstructure after processing. Near-alpha alloys contain a large volume of hexagonal-close packed (HCP) alpha phase in a matrix of transformed beta. Although the exact microstructure is heavily dependent on in-process work and heat treatments, colony formations are a common feature. Colonies form when the alloy is cooled from the beta transus allowing primary alpha ribs to nucleate and grow. A Burgers orientation relationship exists between the body-centered cubic (BCC) beta phase and the HCP alpha phase, resulting in twelve possible crystallographic variants for the alpha ribs^{10, 15}.

$$(101)_{\beta} \parallel (0001)_{\alpha} \quad [1\bar{1}\bar{1}]_{\beta} \parallel [2\bar{1}\bar{1}0]_{\alpha}$$

Figure 2.1 illustrates the orientation relationship for Ti-6242Si as experimentally observed by Neeraj *et al.*¹⁰ As seen from the figure, when both the alpha and beta phase are present in a microstructure distinct <a>-type slip vectors may be identified. The HCP slip vector <a₁> is defined by the smallest misalignment between the aforementioned directions (approx 0.7°). Likewise <a₂> is distinguished by the next largest Burgers

vector delta between the two phases (approx 11.1°), while $\langle a_3 \rangle$ lacks a corresponding $\langle 111 \rangle$ vector.

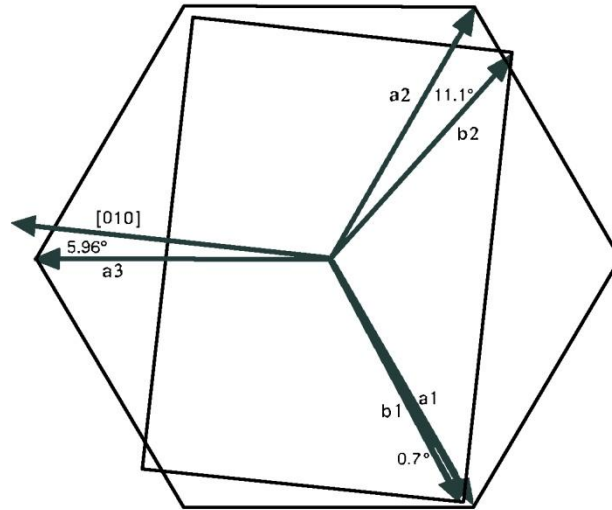


Figure 2.17: Burgers orientation relationship between alpha and beta phases.
Adapted from Neeraj *et al.*¹⁰

The critical resolved shear stress anisotropy between the three line directions is well established for both prismatic and basal slip systems^{5, 10, 15, 16}. Suri *et al.* proposed that the creation of misfit dislocations at the alpha-beta interface during slip transmission between the alpha and beta phases produced interaction stresses which affected each slip-system distinctly¹⁵. Figure 2.2 presents published critical resolved shear stresses for activation of $\langle a \rangle$ -type slip in single colonies of near-alpha or alpha-beta alloys at strain rates near $1 \times 10^{-4} \text{ s}^{-1}$.

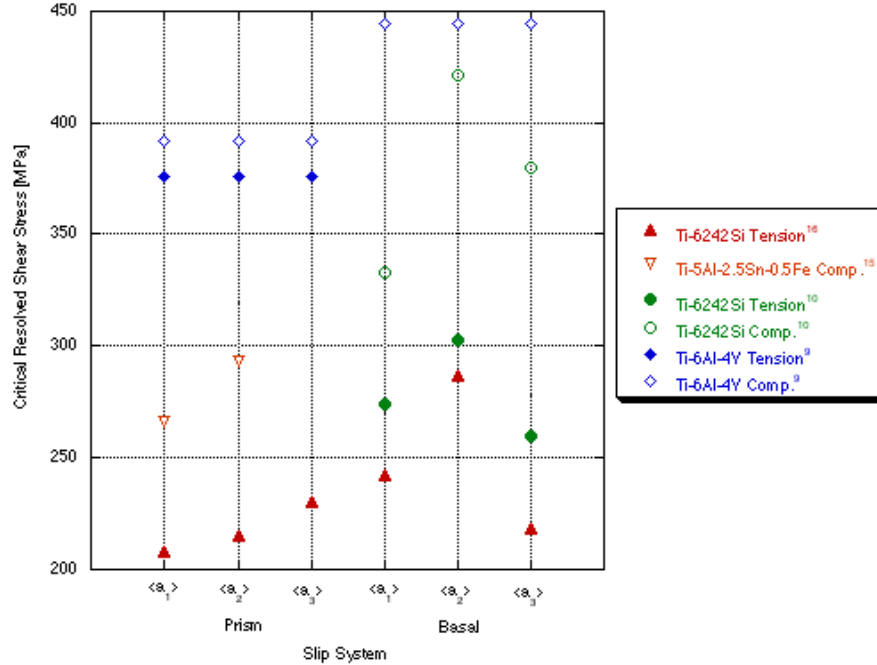


Figure 2.18: CRSS comparison for Ti-6242Si alpha phase slip systems near 298K

The Ti-6Al-4V strengths published by Jones and Hutchinson were obtained from highly textured material – not single colonies – and a distinction was not made among the different alpha-phase orientations during testing⁹. The summary also includes strength values for Ti-6242Si determined by both conventional compression tests and small scale tensile tests^{5, 6, 16}. (It is important to note that the relatively low CRSS data published by Savage *et al.* was based on the proportional limit rather than the 0.2% offset yield strength¹⁶.) As discussed in Section 1.1, the results from these initial micro-tensile tests were questionable. The purpose of this study is to repeat these tests on the updated micro-tensile system at The Ohio State University.

As expected from the single-phase literature, $\langle a \rangle$ -type prismatic slip generally activates at lower stresses than $\langle a \rangle$ -type basal slip, with an exception for the (0001) $\langle a_3 \rangle$

system. The anisotropy trends are identical in all of the compression and tension results where a distinction was made between the different $\langle a \rangle$. A consistent strength differential exists between the published compression and tension resolved shear strengths, wherein the tensile resolved shear strength is lower than the same system in compression.

2.2: Experimental Procedure

In order to thoroughly characterize the tensile response of $\langle a \rangle$ -type slip in single colonies, micro-tensile samples were created from a rod of near-alpha Ti-6Al-2Sn-4Zr-2Mo-0.1Si (Ti-6242Si). Large colonies, ranging in size from 5 to 25 mm, were grown using a vertical float-zone technique at Wright Patterson Air Force Base, courtesy of Dr. Michael Uchic. The alloy composition can be found in Table 2.1; further crystallographic information specific to the material used in this study is discussed by Savage⁵.

Element	Composition [wt%]
Al	6.01 ± 0.005
Sn	1.96 ± 0.0035
Zr	4.01 ± 0.005
Mo	1.96 ± 0.0035
Si	0.10 ± 0.005
O	0.131 ± 0.008
N	0.012 ± 0.003

Table 2.6: Alloying content of Ti-6242Si single colony rod⁵

Six unique slip systems were selected for micro-tensile testing: $\{10\bar{1}0\}\langle a_1 \rangle$, $\{10\bar{1}0\}\langle a_2 \rangle$, $\{10\bar{1}0\}\langle a_3 \rangle$, $(0001)\langle a_1 \rangle$, $(0001)\langle a_2 \rangle$, and $(0001)\langle a_3 \rangle$. All of the samples were oriented to maximize the Schmid factor on the desired slip plane. The polished face

of the samples contained both the normal to the slip plane and the shear vector. Details of the sample preparation process are given in Appendix A. Single colonies were tested in the as-received condition; no heat treatments were performed on the samples. The very slow growth rates experienced by the colony crystal during growth ensure a well-developed short-range-order state in the alpha phase. At least one sample was monotonically loaded at each of the following rates: $1.7 \times 10^{-4} \text{ s}^{-1}$, 5.3×10^{-4} , and 9.7×10^{-4} . The methods used to calculate critical resolved shear stress, hardening rate, and rate sensitivity are discussed in Section 1.2.

2.3: Micro-Tensile Test Results

2.3.1: Prismatic Slip Observations

Similar to prismatic slip in alpha phase single crystals, $\{10\bar{1}0\}\langle a \rangle$ slip in the two-phase alloy occurred in fine, homogeneous bands across the majority of the gage length. A comparison of the $\langle a_1 \rangle$ and $\langle a_2 \rangle$ prismatic slip traces is shown in Figure 2.3. (Unfortunately, the samples for $\{10\bar{1}0\}\langle a_3 \rangle$ slip were not appropriately oriented for characterization of this system.) $\langle a_1 \rangle$ slip can be seen intersecting the beta ribs at an acute angle, with a few instances of beta rib shear offset. The incident angle was much larger for the $\{10\bar{1}0\}\langle a_2 \rangle$ oriented sample, and shear offsets of the beta rib are numerous. The slip character and line spacing in each image are consistent with SEM micrographs presented by Savage for Ti-6242Si micro-tensile samples with the same orientations⁵.

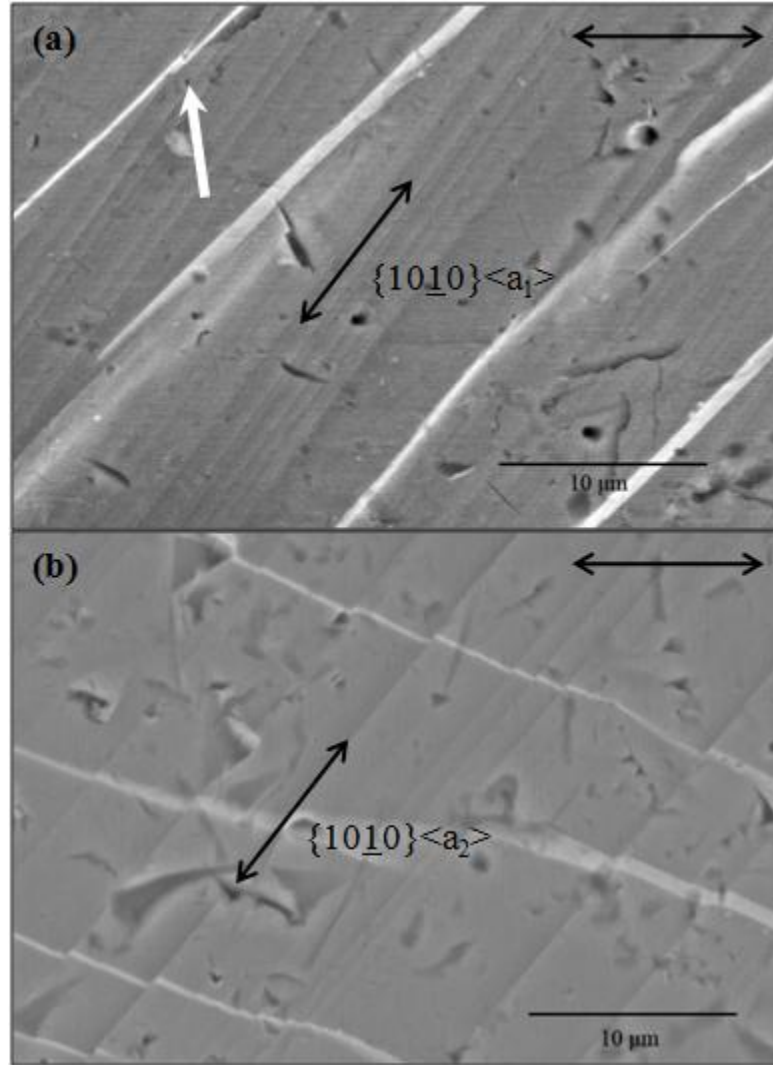


Figure 2.19: Backscattered SEM images of (a) $\langle a_1 \rangle$ prism slip morphology of sample tested at $1.7 \times 10^{-4} \text{ s}^{-1}$ to a failure strain of 28.9% and (b) $\langle a_2 \rangle$ prism slip morphology of sample tested at $1.7 \times 10^{-4} \text{ s}^{-1}$ to a failure strain of 17.6%

True stress-strain curves for the samples oriented for $\langle a_1 \rangle$ and $\langle a_2 \rangle$ prismatic slip are shown in Figure 2.4 and Figure 2.5, respectively. It should be noted that the monotonic strain rate tests shown in these figures were based on VIC2D strain measurements, and as such do not contain the near-failure portion of the curve (see Section A.1.1). The magnitude of softening was quite small for both prism systems.

Table 2.2 presents the mechanical properties for the two-phase prismatic slip micro-tensile tests. The strain rate sensitivities as calculated at one percent plastic strain are $m = 0.030$ and $m = 0.008$ for the $\{10\bar{1}0\}\langle a_1 \rangle$ and $\{10\bar{1}0\}\langle a_2 \rangle$ systems, respectively.

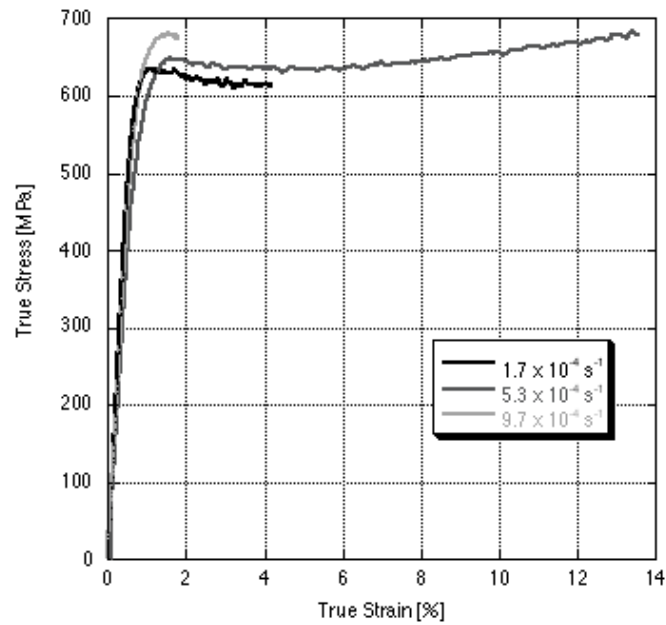


Figure 2.20: True stress-strain curves for samples oriented for $\langle a_1 \rangle$ prismatic slip

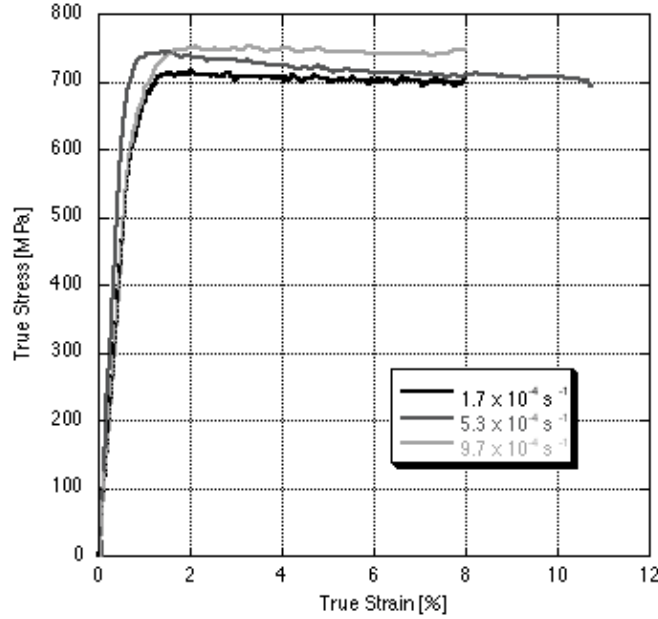


Figure 2.21: True stress-strain curves for samples oriented for $\langle a_2 \rangle$ prismatic slip

Slip System	Strain Rate [s^{-1}]	0.2% Offset Yield [MPa]	Upper Yield Point [MPa]	CRSS [MPa]	Total Strain [%]	n [$\times 10^{-2}$]
$a_1 \{10\bar{1}0\}$	1.7×10^{-4}	607	631	303	28.9	-2.6
	5.3×10^{-4}	562	640	281	25.6 **	-1.8
	9.7×10^{-4}	625	670	313	19.0 **	-
$a_2 \{10\bar{1}0\}$	1.7×10^{-4}	642	702	319	17.6	-1.2
	1.7×10^{-4}	650	728	324	4.5 *	-0.8
	5.3×10^{-4}	681	736	339	17.8	-2.8
	9.7×10^{-4}	666	738	332	15.6	-0.9

Table 2.7: Mechanical properties of Ti-6242Si samples oriented for prismatic slip

* Sample was stopped prematurely to examine the small strain region.

** Sample was stopped before failure to ensure total strain measurement using the optical system.

2.3.1: Basal Slip Observations

The results of the monotonic strain rate micro-tensile tests for Ti-6242Si samples oriented for basal slip are presented in Figures 2.6 through 2.8, as well as Table 2.3. As compared to the single phase basal slip, significantly more moderate softening – and

sometimes even slight hardening – was observed across all three sets of samples. The basal system strain rate sensitivities as calculated from one percent plastic strain are $m = 0.125$ for $(0001)\langle a_1 \rangle$, $m = 0.115$ for $(0001)\langle a_2 \rangle$, and $m = 0.140$ for $(0001)\langle a_3 \rangle$.

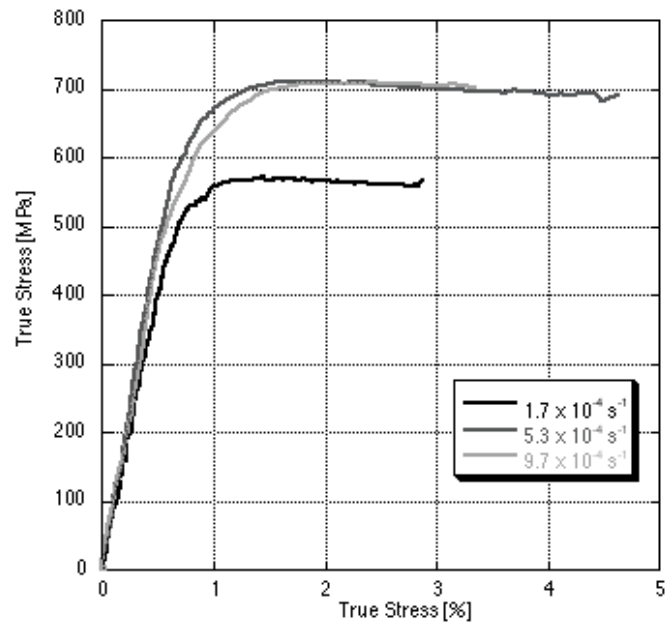


Figure 2.22: True stress-strain curves for samples oriented for $\langle a_1 \rangle$ basal slip

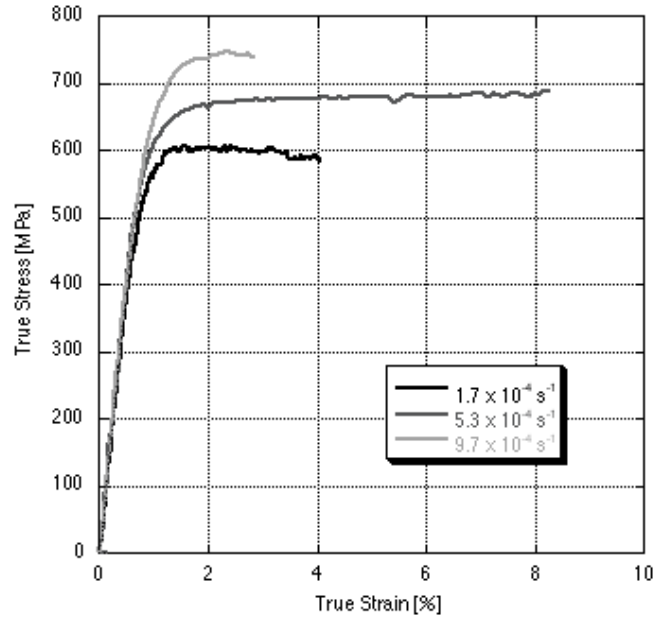


Figure 2.23: True stress-strain curves for samples oriented for $\langle a_2 \rangle$ basal slip

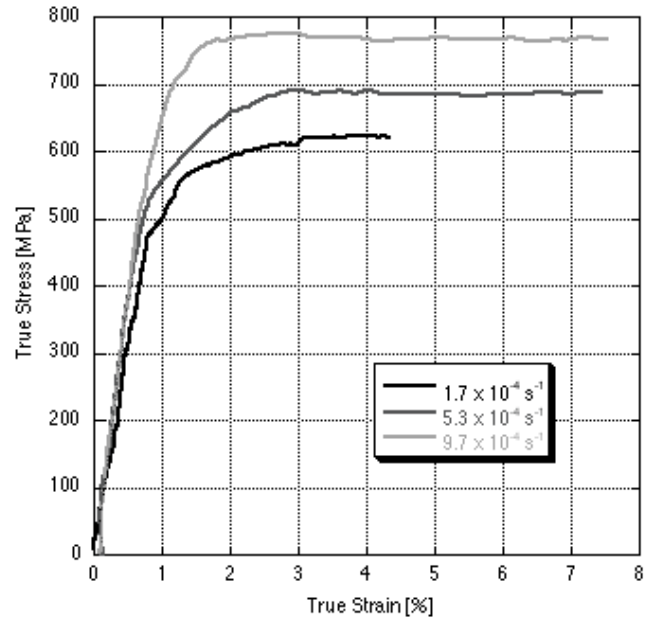


Figure 2.24: True stress-strain curves for samples oriented for $\langle a_3 \rangle$ basal slip

Slip System	Strain Rate [s^{-1}]	0.2% Offset Yield [MPa]	Upper Yield Point [MPa]	CRSS [MPa]	Total Strain [%]	n [$\times 10^{-2}$]
a ₁ (0001)	1.7×10^{-4}	540	570	270	9.8	-1.2
	5.3×10^{-4}	640	712	320	12.0	-0.6
	9.7×10^{-4}	611	710	306	5.5	1.9
a ₂ (0001)	1.7×10^{-4}	555	576	277	14.9	-0.4
	1.7×10^{-4}	576	693	287	3.2 *	-
	5.3×10^{-4}	593	657	296	11.8	1.2
	9.7×10^{-4}	630	730	314	6.5	-
a ₃ (0001)	1.7×10^{-4}	558	615	278	10.0	2.2
	5.3×10^{-4}	538	671	268	19.3 †	-0.4
	9.7×10^{-4}	670	755	334	40.2 †	-0.2

Table 2.8: Mechanical properties of Ti-6242Si samples oriented for basal slip

* Sample was stopped prematurely to examine the small strain region.

† Sample failed through a combination of shear and tearing.

SEM images of the micro-tensile sample surfaces, Figures 2.9 through 2.11, showed distinctly different slip morphology than the fine traces observed by Savage⁵. Instead, well-defined $\langle a \rangle$ -type basal slip lines can be seen clearly in the alpha phase. $\langle a_1 \rangle$ and $\langle a_3 \rangle$ basal slip have indistinct interaction with the beta phase; however, slip transmission was observed frequently at the alpha-beta interface for (0001) $\langle a_2 \rangle$ oriented samples. Secondary slip was activated on both the $\langle a_1 \rangle$ and $\langle a_3 \rangle$ basal samples in the high strain regions near the shear fracture face, as seen in Figure 2.9(b) and Figure 2.11. Presumably, the secondary slip observed in these single colony samples is similar to the secondary slip regions which activated in the single phase samples oriented for basal slip. Savage observed similar secondary slip region on a sample oriented for $\langle a_2 \rangle$ basal slip, although it was not seen specifically in this study⁵.

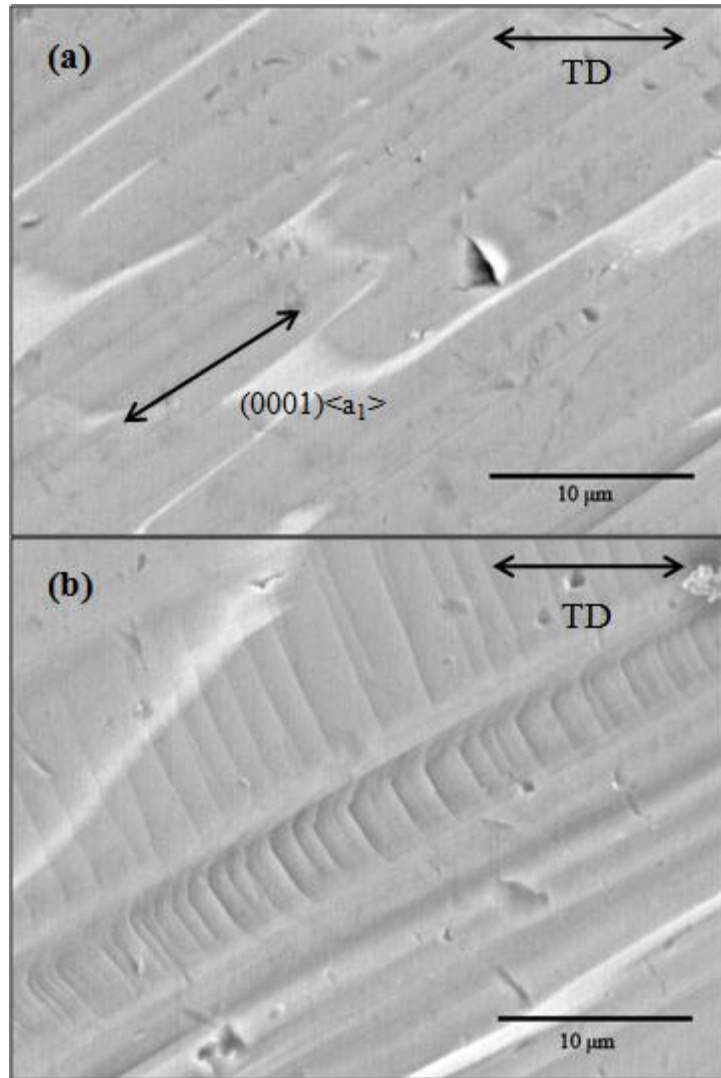


Figure 2.25: Backscatter SEM images illustrating (a) single slip regime of $\langle a_1 \rangle$ basal slip in sample tested at $1.7 \times 10^{-4} \text{ s}^{-1}$ to a failure strain of 9.8% and (b) evidence of secondary slip near shear failure in the same sample

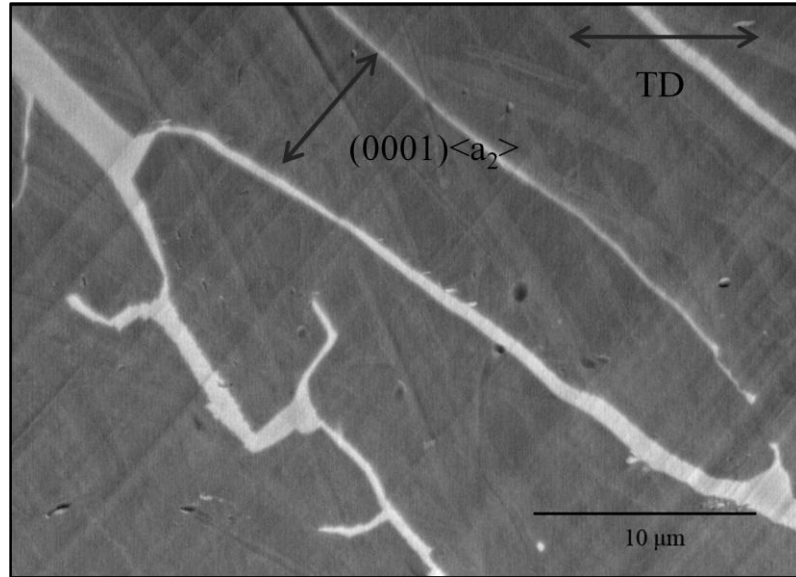


Figure 2.26: Backscatter SEM image of (0001)⟨a₂⟩ slip morphology in sample tested at $1.7 \times 10^{-4} \text{ s}^{-1}$ to a failure strain of 14.9%

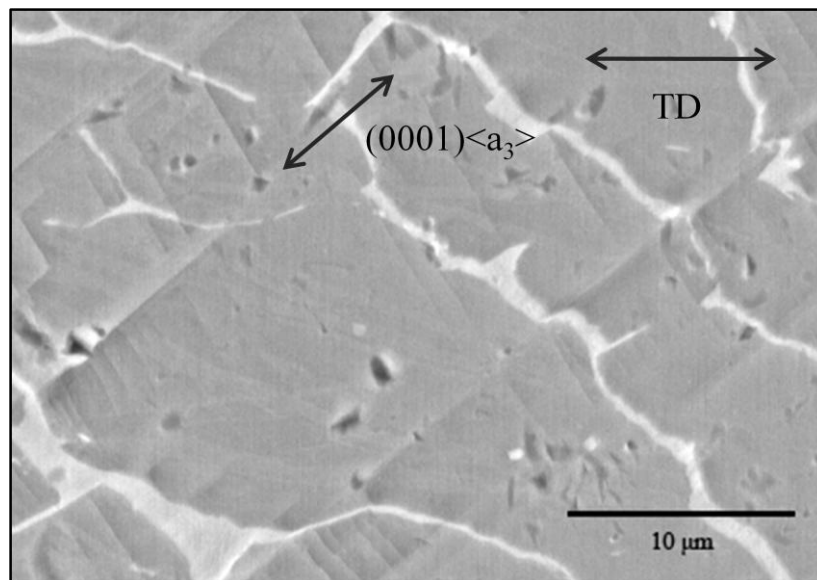


Figure 2.27: Backscatter SEM image of (0001)⟨a₃⟩ slip morphology in sample tested at $1.7 \times 10^{-4} \text{ s}^{-1}$ to a failure strain of 10.0%.

2.4: Discussion

Figure 2.12 compares the results of this study to the published resolved shear strengths of near-alpha and alpha-beta titanium single colonies oriented for activation of a select $\langle a \rangle$ -type slip. Although the strength magnitudes of the present study were higher than expected, the trend observed in the anisotropy of the prismatic slip samples was consistent with both the tension work performed by Savage and the compression study completed by Suri *et al.*^{15, 16} Conversely, the strength values for the basal slip systems corresponded well to the other tensile studies on Ti-6242Si; however, the asymmetry trend did not agree with the published data. The resolved shear strength for the (0001) $\langle a_3 \rangle$ was higher than anticipated based on the aforementioned studies.

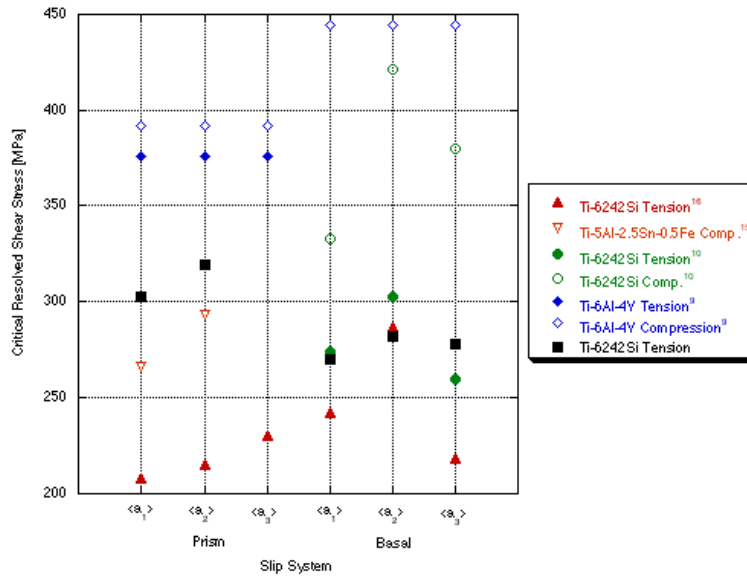


Figure 2.28: Tension vs. compression asymmetry for alpha phase slip systems in dual phase single colonies

The response parameters of the single colony micro-tensile tests are presented in Table 2.4. Softening was observed in the majority of the two-phase tensile tests, although the softening rates were relatively minimal. In both compression and tension, the magnitude of the hardening rate increased with increasing mis-orientation between the alpha phase and beta phase Burgers vectors. The single colony tensile basal rate sensitivities, similar to the single crystal data, were much higher than the corresponding compression values. While the tensile $\{10\bar{1}0\}\langle a_1 \rangle$ rate sensitivity closely approximated the compression data, the low $\{10\bar{1}0\}\langle a_2 \rangle$ value was a direct result of the odd response of the $5.3 \times 10^{-4} \text{ s}^{-1}$ stress-strain curve.

Slip System	n_{TEN}	n_{COMP}	m_{TEN}	m_{COMP}
$\{10\bar{1}0\}\langle a_1 \rangle$	-0.026	0^6	0.030	0.025^6
$\{10\bar{1}0\}\langle a_2 \rangle$	-0.012	0.028^6	0.008	0.025^6
$(0001)\langle a_1 \rangle$	-0.012	0.017^6	0.125	0.025^6
$(0001)\langle a_2 \rangle$	-0.004	0.027^6	0.115	0.028^6
$(0001)\langle a_3 \rangle$	0.022	0.034^6	0.140	0.024^6

Table 2.9: Summary of hardening and rate sensitivities for Ti-6242Si alpha phase slip systems in tension and compression. Hardening rates are provided for tests at strain rate near $1.7 \times 10^{-4} \text{ s}^{-1}$; tension rate sensitivity values were calculated at one percent plastic strain.

The deformed micro-tensile samples from this study should be further characterized to identify all activated slip systems, as well as examine slip transmission between the phases. Additional samples may also be aged to study the effect of beta rib thickness, alpha lath size, or the presence of secondary alpha on $\langle a \rangle$ -type slip transmission.

References

1. Partridge, P. The Crystallography and Deformation Modes of Hexagonal Close-Packed Metals. *Metallurgical Reviews* **12**, 169-194(1967).
2. Williams, J.C., Baggerly, R.G. & Paton, N.E. Deformation Behavior of HCP Ti-Al Alloy Single Crystals. *Metallurgical and Materials Transactions A* **33**, 837-850(2002).
3. Sakai, T. & Fine, M. Plastic Deformation of Ti-Al Single Crystals in Prismatic Slip. *Acta Metallurgica* **22**, 1359-1372(1974).
4. Sakai, T. & Fine, M. Basal Slip of Ti-Al Single Crystals. *Scripta Metallurgica* **8**, 545-548(1974).
5. Savage, M. Microstructural and Mechanistic Study of Low Temperature Creep and Dwell Fatigue in Single Colony Alpha/Beta Titanium Alloys. 339(2000).
6. Brandes, M. Creep, Fatigue, and Deformation of Alpha and Alpha-Beta Titanium Alloys at Ambient Temperature. 442(2008).
7. Girshick, A., Pettifor, D. & Vitek, V. Atomistic simulation of titanium. Part II: Structure of screw dislocations and slip systems in titanium. *Philosophical Magazine* **77**, 999-1012(1998).
8. Ando, S., Takashima, K. & Tonda, H. Molecular dynamics simulation of (c+a) edge dislocation core structure in HCP crystal. *Material Transactions* **37**, 319-322(1996).
9. Jones, I.P. & Hutchinson, W.B. Stress-State Dependence of Slip in Titanium-6Al-4V and Other HCP Metals. *Acta Metallurgica* **29**, 951-968(1961).
10. Neeraj, T. et al. Observation of Tension-Compression Asymmetry in Alpha-Alpha/Beta Titanium Alloys. *Philosophical Magazine* **85**, 279-295(2005).
11. Sharpe, W., Danley, D. & LaVan, D. Microspecimen Tensile Tests of A533-B Steel. *ASTM STP 1329: Small Specimen Test Techniques* 497-512(1998).

12. Dimiduk, D., Uchic, M. & Parthasarathy, T. Size-affected single-slip behavior of pure nickel microcrystals. *Nano* **53**, 4065-4077(2005).
13. Hemker, K.J. & Sharpe, W.N. Microscale Characterization of Mechanical Properties. *Annual Review of Materials Research* 93-126(2007).doi:10.1146/annurev.matsci.36.062705.134551
14. Fisher, E. & Renken, C. Single-Crystal Elastic Moduli and the HCP to BCC Transformation in Ti, Zr, and Hf. *Physical Review* **135**, A482-A495(1964).
15. Suri, S. et al. Room Temperature Deformation and Mechanisms of Slip Transmission in Oriented Single-Colony Crystals of an Alpha/Beta Titanium Alloy. *Acta Metallurgica* **47**, 1019-1034(1999).
16. Savage, M.F. et al. Deformation mechanisms and microtensile behavior of single colony Ti-6242Si. *Materials Science and Engineering A* **321**, 398- 403(2001).
17. Sutton, M., Orteu, J. & Schreier, H. *Image Correlation for Shape, Motion and Deformation Measurements*. Access 321(Springer: New York, NY., 2009).
18. Zupan, M. & Hemker, K. Tension and Compression Testing of Single-Crystalline Gamma Ti-55.5 Pct Al. *Metallurgical and Materials Transactions A* **29**, 65-71(1998).
19. Wu, T. & Smoluchowski, R. A New Criterion for the Occurrence of Slip in Thin Single Crystals. *Physical Review* **78**, 468-469(1950).
20. Dingley, D.J. & Randle, V. Review: Microtexture Determination by Electron Back-scatter Diffraction. *Journal of Materials Science* **27**, 4545-4566(1992).
21. Adams, B.L., Wright, S.I. & Kunze, K. Orientation Imaging : The Emergence of a New Microscopy. *Metallurgical Transactions A* **24**, 819-831(1993).

Appendix A: Experimental Procedure

A.1: Small Scale Tensile Test System

The small scale tensile testing system at the Ohio State University was adapted from a similar apparatus developed by Sharpe *et al.*¹¹. As with conventional testing frames, the system included a fixture to hold the sample, a means by which to displace it, and equipment to measure both the resultant load and displacement. Figure A.1 schematically depicts the current experimental rig used to obtain uniaxial tensile stress-strain curves.

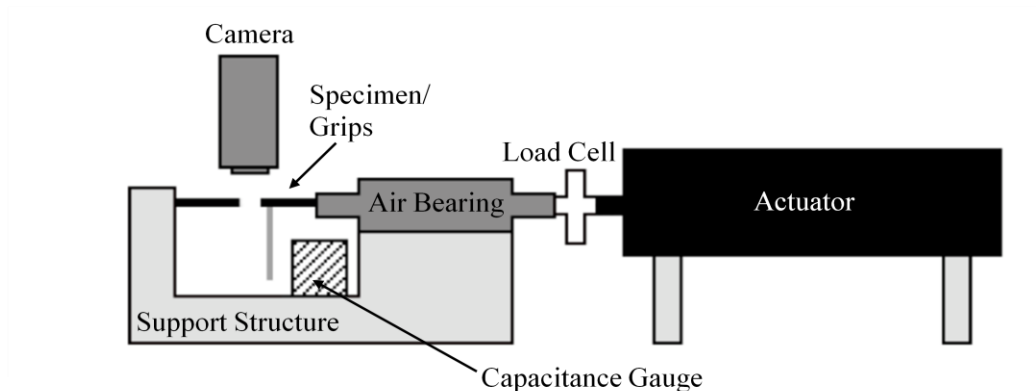


Figure A.29: Illustration of small scale tensile test system

A nested grip mechanism was employed to allow the sample to self-align during pre-loading, prior to the tensile test. The “bowtie” sample geometry mated with a cavity machined into the grips, as shown in Figure A.2. One grip is fixed to a support structure,

while the other is connected through a linear air bearing to the load cell and actuator. A Physik Instrumente (PI) M-238PG motor-controlled screw drive allowed for precise control of the grip placement. The actuator has a total travel range of 50 mm with a resolution of 0.13 microns up to a maximum velocity of 30 mm per second. A Honeywell-Sensotec Model 31 load cell was also placed on the drive train to measure the resultant load. The gauge can measure up to 100 pounds with 0.2% full scale accuracy, and was calibrated in-house by measuring the response to a series of weights hung from the cell. The entirety of the small scale tensile system sits on a Technical Manufacturing Corporation (TMC) Clean Top II damping table to reduce vibrations from the environment.

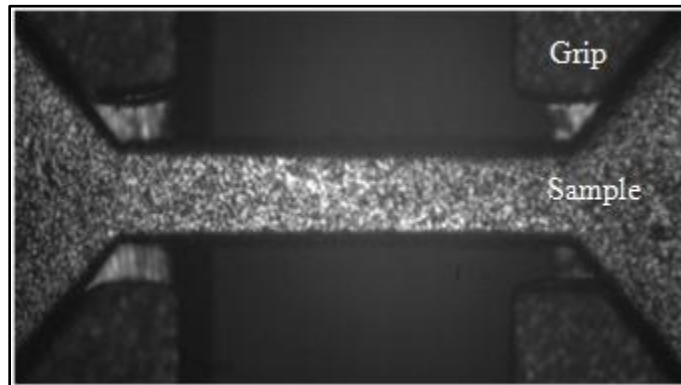


Figure A.30: "Bowtie" specimen with speckle pattern preloaded in grips

Strain measurement on a small scale specimen leads to unique challenges not seen in conventional loading frames; therefore, non-contact extensometry must be used to avoid altering the response of the material. An ADE Technologies Model 4810 capacitance gauge was used to observe the grip position during a tensile test. However,

this measurement did not accurately reflect the strain experienced by the sample due to compliance in the system. Therefore, a PixeLINK PL-A782 camera was placed above the sample at a large enough distance to capture the entire gauge length of the sample during deformation. A LabVIEW program was written to acquire an image at fixed intervals, as well as record the corresponding test time and load cell measurement. The strain experienced by the sample was analyzed using VIC2D, a commercially available digital image correlation (DIC) software. DIC is discussed further in the following section.

The micro-tensile system was aligned through a series of tensile tests where VIC2D was used to ensure the elimination of bending stresses. A load-unload test was also run to confirm that the elastic region of a sample was constant over a range of strain rates.

A.1.1: Digital Image Correlation

Two-dimensional digital image correlation (2D-DIC) is an effective technique or quantitative analysis of in-plane surface deformation¹⁷. A full-field displacement map is created by tracking subsets of the initial image, taken prior to loading, to an image taken after inducing deformation. The process begins by applying a random, isotropic pattern to the surface of the sample. A Gaussian grayscale distribution is desirable for effective spatial resolution, and a rough rule of thumb states that the average feature size in the pattern should cover a 3-by-3 pixel area. Any image files obtained during testing may be treated as a pixel array of grayscale values. From this information, the size of the image subset is defined such that a unique grayscale variation exists within each square area.

The distance between the centers of two adjacent subsets, or step size, controls the total number of subsets processed. An iterative algorithm is used to minimize the sum of squares deviation of the grayscale intensities between a subset in the initial image and the corresponding deformed subset. A higher-order polynomial shape function is applied to an individual subset to calculate rigid body translation and rotation, as well as deformation. The shape function also allows for interpolation between pixels, resulting in sub-pixel accuracy in the deformation map. Sutton, Orteu, and Schreier present a comprehensive and detailed discussion on the theory supporting digital image correlation¹⁷.

VIC2D, offered by Correlated Solutions Inc., contains a robust algorithm to efficiently compare a large quantity of subsets across numerous images. To obtain the strain across the entire gage length, a “virtual extensometer” method was used. The movement of two pixels, one on each end of the gage section, was tracked across the test images, and this measured extension was later converted to strain. Slight perturbations of the imaging system resulted in errors in the precision of the small strain calculations. In successive images the sample can be seen shifting by a few pixels, which affected strain measurements at very low strains ($< 0.2\%$). Once the sample locally extended more than the magnitude of these variations, VIC2D was readily able to track displacements. Additionally, significant local plastic deformation on certain samples created a loss in contrast of the surface pattern making in-situ VIC2D strain measurements impossible, particularly near failure. For these tests, the samples results are marked accordingly, and the total strain is presented.

A.2: Generic Sample Preparation

Small scale testing offered a unique opportunity to create single crystal or single colony samples out of material with sufficiently large grains. The sample preparation process began by dividing polycrystalline titanium rods into individual crystals. One face of each crystal was mechanically prepared using silicon carbide abrasive discs before being vibratory polished with 0.02-micron colloidal silica for up to 48 hours. The crystallographic orientation of the crystal was determined using electron backscatter diffraction (EBSD). One millimeter slices were cut parallel to desired planes on a Southbay Model 660 slow-speed saw; the exact orientations are discussed in their respective chapters. Taking care to keep the slices as parallel as possible to the cut face, the slices were then polished on an Allied Multiprep to a final slice thickness of 300-400 microns. The orientation of the slices was confirmed again prior to heat treatment.

For material requiring heat treatment, the slices were wrapped in tantalum foil before being encapsulated in clean quartz tubes along with a secondary piece of titanium foil to getter oxygen. The encapsulation tube was evacuated to 10^{-6} torr before being backfilled with 1/6 atm high purity argon. The sample was then placed in a pre-heated tube furnace and monitored with a thermocouple to ensure the desired temperature was reached. The specific details of the heat treatments are presented in the relevant chapters.

Once the slices had been adequately prepared, the samples were sent to Oxford Laser Inc. for sample cutting. The work was done with a green nanosecond laser with a pulse duration of 25ns operating at a repetition rate of 10 kHz. The focused laser spot was

approximately 10 microns in diameter. Laser cutting offers an improved cross-sectional profile when compared to the punch EDM samples used by Savage⁵. Figure A.3 demonstrates the differences seen between the cross-sections of the two cutting methods. However, it is important to note that a significant recast layer of approximately six microns was observed on the perimeter of the samples (shown in Figure A.4).

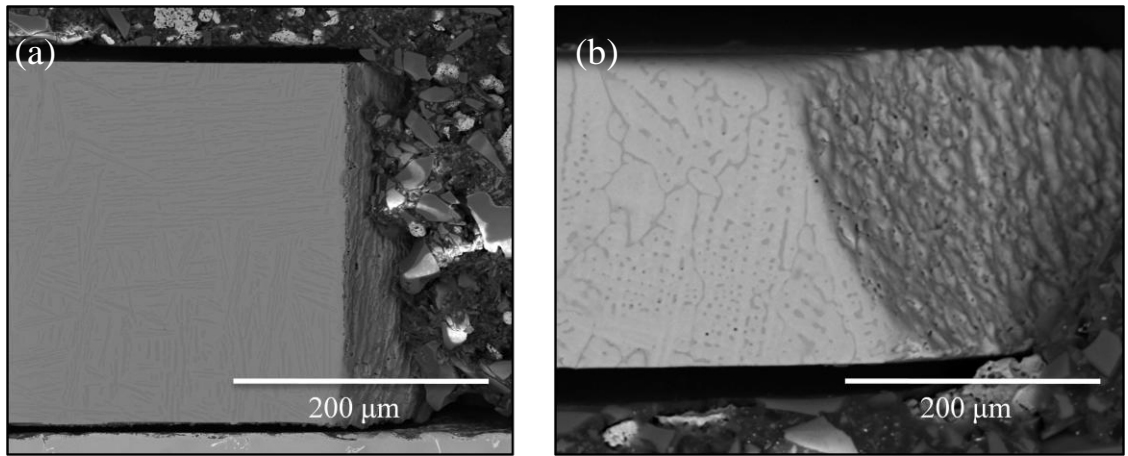


Figure A.31: (a) Square cross-section of laser cut sample; (b) Tapered cross-section of punch EDM sample

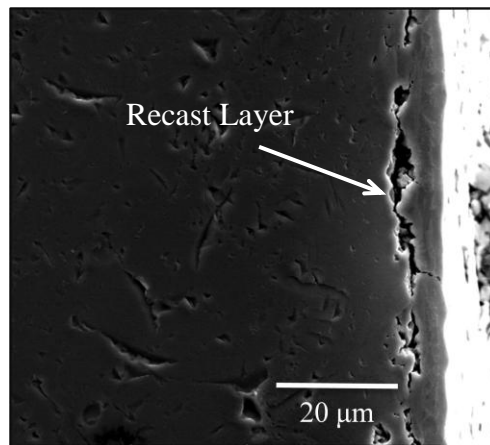


Figure A.32: Rough edge and recast layer on sample perimeter (approx. 6 μm)

Once returned, the samples were lightly ground using 1200 grit silicon carbide paper and polished to remove any surface damage, although small divots can still be seen on some samples. Directly before testing, a “speckle” pattern was applied by sprinkling printer toner over the sample to achieve an optimal grayscale distribution, as discussed in Section A.1.1. The sample shown in Figure A.2 shows a typical speckle pattern.

A gage section of $300\mu\text{m} \times 300\mu\text{m} \times 1700\mu\text{m}$ was successfully used in previous micro-tensile tests^{5, 16, 18}. A square cross-section ensures that the desired slips are activated, and not biased towards the system with the shortest slip path across the crystal, as initially observed by Wu and Smoluchowski¹⁹. The sample geometries are shown in Figure A.5. Tensile A was used for the majority of the micro-tensile samples, while Tensile B was used for orientations where large plastic deformation was expected to ensure that the material outside of the gage section did not deform.

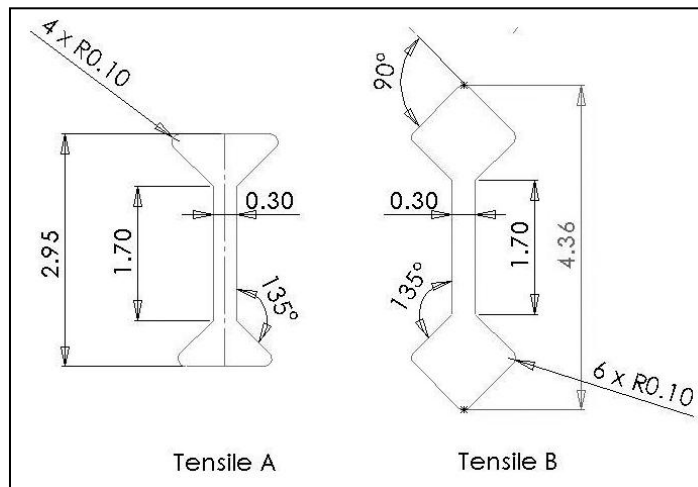


Figure A.33: Micro-tensile sample geometries. All dimensions are in millimeters.

A.3: Characterization

Throughout the sample preparation and testing process, both optical and scanning electron microscopy were performed frequently. Two scanning electron microscopes (SEM) were used for microstructure characterization: an FEI XL-30 ESEM FEG and an FEI Quanta. The majority of the work was performed on the ESEM due to its higher resolution capabilities. All SEM images were obtained with the backscatter electron detector, 20kV, and a spot size of 5 unless otherwise noted. To determine crystallographic orientation, electron backscatter diffraction (EBSD) analysis was performed using TSL Orientation Imaging Microscopy (OIM) Data Collection and OIM Analysis software. Detailed overviews of the EBSD technique are presented by Dingley and Randle²⁰ and Adams *et al*²¹. To measure the exact crystallographic orientation of the samples, an EBSD map of a (001) silicon wafer attached to the same SEM stub was obtained immediately prior to data collection on each sample. In order to act as an electronic material substrate, extremely tight orientation tolerances are required when producing silicon wafers. Therefore, the corrections required to bring the silicon wafer data in line with its expected orientation can also be applied to the titanium samples to eliminate any small errors in the EBSD data collection system.

All transmission electron microscopy was performed by Matt Brandes on a FEI Tecnai TF20 transmission electron microscope (TEM). TEM foils were created using an FEI Helios focused ion beam (FIB) outfitted with a Sidewinder Ga⁺ ion column and an Omniprobe in-situ lift out mechanism. The process began by applying a three micron thick protective platinum layer to an area of interest on the micro-tensile sample surface.

Trenches, approximately 15 microns deep and 30-50 microns wide, were cut on either side of the desired region to create a foil. Once the foil was plucked and welded to a copper grid, it was thinned first to 300 nm with 30 kV ions and then to 100 nm using a 5 kV beam. Each side of the foil was subsequently cleaned at 900 eV and 500 eV with Ar⁺ ions in a Fischione 1040 NanoMill with a current of 120 pA. The Tecnai was operated in Scanning TEM, or STEM, mode at 200 kV. The foil was tilted to the appropriate two-beam condition, and imaged with a Yg-dectector at a camera length of approximately one meter. The bright field images were acquired using an 8-10 mrad convergence angle.

Appendix B: Nomenclature

ε = True Strain

$\dot{\varepsilon}$ = True Strain Rate

ε_{pl} = True Plastic Strain

m = Strain Rate Sensitivity

n = Hardening Rate

σ = True Stress